
Using persistent homology to understand dimensionality reduction in resting-state fMRI

Ty Easley

Mallinckrodt Institute of Radiology
Washington University in St. Louis
tyoeasley@wustl.edu

Kevin Freese

IBM *
kmfreese@protonmail.com

Elizabeth Munch

Dept of Computational Mathematics,
Science and Engineering
Dept of Mathematics
Michigan State University
muncheli@msu.edu

Janine Bijsterbosch

Mallinckrodt Institute of Radiology
Washington University School of Medicine
janine.bijsterbosch@wustl.edu

Abstract

Despite much attention, the comparison of reduced-dimension representations of high-dimensional data remains a challenging problem in multiple fields, especially when representations remain high-dimensional compared to sample size. We offer a framework for evaluating the topological similarity of high-dimensional representations of very high-dimensional data, a regime where topological structure is more likely captured in the distribution of topological “noise” than a few prominent generators. Treating each representational map as a metric embedding, we compute the Vietoris-Rips persistence of its image. We then use the topological bootstrap to analyze the re-sampling stability of each representation, assigning a “prevalence score” for each nontrivial basis element of its persistence module. Finally, we compare the persistent homology of representations using a prevalence-weighted variant of the Wasserstein distance. Notably, our method is able to compare representations derived from different samples of the same distribution and, in particular, is not restricted to comparisons of graphs on the same vertex set. In addition, representations need not lie in the same metric space. We apply this analysis to a cross-sectional sample of representations of functional neuroimaging data in a large cohort and hierarchically cluster under the prevalence-weighted Wasserstein. We find that the ambient dimension of a representation is a stronger predictor of the number and stability of topological features than its decomposition rank. Our findings suggest that important topological information lies in repeatable, low-persistence homology generators, whose distributions capture important and interpretable differences between high-dimensional data representations.

1 Introduction

Comparisons of reduced-dimension representations of high-dimensional data have received much attention in the field, but remain a difficult problem in many application domains and problem regimes. Approaches to characterize both the quality^{1,2} and properties³⁻⁷ of data representation methods span many disciplines, problem contexts, and formalisms. The ongoing refinement of methodologies in persistent homology has offered several promising approaches to this problem over recent years.⁸⁻¹⁰

*The views expressed herein are those of the author and do not represent the views of IBM

Many of these investigations have emphasized problem settings where representation dimensions were low enough to be visualized (and could therefore be inspected), but many important representation problems do not fall within this regime. In addition, due to difficulties in defining statistical structures on the space of persistence diagrams,^{11,12} earlier such approaches have not been equipped with the ability to make statistical claims about differences between representations. The recent introduction of the topological bootstrap^{13,14} allows the articulation of a robust, flexible formalism for the comparison of data representations that incorporates statistical information about the stability of topological features. Our goal in this paper is to describe such a formalism and explore its application to a large cohort of neuroimaging data.

1.1 Motivation and application in neuroimaging

Our approach to the problem of representation comparison rises from repeated efforts to characterize the impact of analytical flexibility in neuroimaging analysis pipelines. Analytical flexibility is a major challenge in psychology and neuroimaging that encompasses the wide range of acceptable analysis steps and parameter decisions available to researchers.¹⁵ Analytical flexibility leads to tens of thousands of different versions of valid analysis pipelines, with extensive variability in results.¹⁶ This variability tightly constricts cross-pollination of findings and ideas and has a siloing effect on neuroimaging research as a whole.

These challenges are especially difficult to characterize and address in resting-state functional neuroimaging, where feature sets differ in both size (depending on parcellation/network definition) and structure (depending on the feature choice).¹⁷ To meet these domain-specific difficulties, our method emphasizes robustness to high-dimensional noisy data, flexibility in feature type and ambient dimension, and the ability to make claims on the statistical significance of differences between representations.

The major novel contribution of this work is to develop a mathematical framework that enables robust and generalizable statistical comparisons between resting state neuroimaging features sets that differ in size and nature. Our framework is built on persistent homology, and we employ it on a large neuroimaging dataset.

1.2 Prior and related work

Our work builds on prior efforts using persistent homology to characterize reduced-dimension data representations. Several prior works consider the recovery of a known manifold and propose quality metrics derived from persistent homology. Paul and Chalup⁹ compare DR methods while varying manifold complexity, measuring performance by the similarity of pre- and post-DR Betti numbers as a function of sampling density. Rieck and Leitte⁸ compute the Wasserstein distance between source- and representation-space persistence diagrams as a metric of embedding quality. Both studies demonstrate that persistence-based quality metrics produce desirable representations, constituting a promising set of baseline experiments in low-dimensional and synthetic manifolds.

We extend their problem framing to consider unknown source manifolds of very high dimension, whose representations also have high dimension. Our problem regime introduces several critical difficulties: both source and target dimensions are much larger than can be visualized, concentration of measure makes measures in the source data space either unreliable or uninformative, and persistence structure is more likely captured in the distribution of near-diagonal “noise” than a few prominent generators. By utilizing the topological bootstrap^{13,14} to measure the re-sampling stability of homology generators, we believe our method offers some solutions to these challenges.

Our approach is also closely related to the Representation Topology Divergence^{10,18} (RTD), but is constructed around a different motivating problem and, correspondingly, makes different trade-offs. The RTD quantifies topological differences between different embeddings of the same point cloud. For a fixed vertex set V , two embeddings (realized by graphs G, G' on V with different edge weights) are topologically contrasted via the *R-cross barcode*, a module whose persistence intervals measure the filtrations for which each nontrivial generator in G' is not yet born in G . The R-cross barcode is an insightful measurement that gives granular and precise information about topological differences in representation.

Our method was built around a different use-case than the RTD, which was designed to inspect neural net representations, and takes some corresponding departures. First, the R-cross barcode is computed via an augmented graph on the doubled vertex set $V \times V$, which is (perhaps prohibitively) computationally costly on some large datasets. This is especially relevant when employing the topological bootstrap, which is compatible with the R-cross barcode, since it also computes the image persistence via an augmented distance matrix. Unfortunately, it is likely that the R-cross barcode is fairly unstable in our "topologically noisy" regime: in high dimensions, we expect to see most topological structure represented by the distribution of low-persistence generators near the diagonal. Lastly, the R-cross barcode is only valid on families of representations that map from the same vertex set: this is not true of our method, which requires only that vertices be generated by uniformly distributed samples from the same manifold and can, e.g., compare graphs on vertex sets of different size.

Finally, we also note that our work joins previous work, such as curvature detection¹⁹ and distributed persistence,²⁰ in emphasizing the topological structure captured by distributions of low-persistence generators. Due to concentration of measure at high dimensions, low-dimensional homology generators are unlikely to show high persistence in any but the simplest of high-dimensional manifolds, suggesting that near-diagonal persistence distributions may contain important topological structure in the high-dimensional regime. We believe our work adds to a growing consensus that "cycles with low persistence may carry meaningful structure"¹³ in high-dimensional, real-world data. Our contributions in the present study are as follows:

1. A flexible and general framework for topological comparison of data representations, applicable to any data that admits a Vietoris-Rips filtration;
2. A careful characterization of the impact of generator retest reliability on measurements of topological difference;
3. Application to real neuroscience data over a diverse slice of widely used neuroimaging representation algorithms, which realize a high-dimensional representation regime that is common in many use cases.

2 Methods

2.1 Theoretical framework

Our approach is motivated by the problem of tracing differences between representations of functional neuroimaging data. We begin by imagining a functional neuroimaging dataset as an N -tuple $\widehat{S} = (s_1, \dots, s_N)$ of random draws from an unknown distribution \mathcal{P} on some compact orientable manifold \mathcal{S} , represented by its fixed embedding in a very high-dimensional ambient space \mathbb{R}^D . The unknown distribution \mathcal{P} reflects the sampling bias introduced by any collection method (e.g., along racial, gendered, and socioeconomic strata), and it is an important conceptual concession to the nonidealities of sampling present in any dataset. However, any smooth distribution \mathcal{P} on \mathcal{S} is realizable as the uniform distribution on another (likely diffeomorphic) manifold $\mathcal{S}' \subset \mathbb{R}^D$, so we will assume without loss of generality that \widehat{S} is uniformly sampled from \mathcal{S} . In this model, \mathcal{S} is the set of possible neuroimaging scans, D is the number of float measurements in a given scan, and N is the number of scans in a given dataset; in our dataset, $D \approx 10^8$ and $N \approx 10^3$ (see Section 2.3).

We define a **representation** (or brain representation) as a function $\varphi : \widehat{S} \rightarrow \mathbb{R}^d$ admitting a smooth extension $\tilde{\varphi}$ to \mathcal{S} such that $\tilde{\varphi}$ is unique in some neighborhood of \widehat{S} , up to multiplication by a nonvanishing C^∞ function. Furthermore, we allow $\widehat{S}_\varphi = \varphi(\widehat{S})$ to be equipped with a nonnegative, symmetric **dissimilarity function** $\delta_\varphi : \widehat{S}_\varphi \times \widehat{S}_\varphi \rightarrow \mathbb{R}$. Set $\mathcal{S}_\varphi = \tilde{\varphi}(\mathcal{S})$, so that the following diagram

commutes:

$$\begin{array}{ccc}
 \widehat{\mathcal{S}} & \xrightarrow{\varphi} & \widehat{\mathcal{S}}_{\varphi} \\
 \downarrow & & \downarrow \\
 \mathcal{S} & \xrightarrow{\tilde{\varphi}} & \mathcal{S}_{\varphi}
 \end{array}$$

The construction above articulates several desirable properties in our problem context. The requirement that φ admit a unique (modulo $C_{\times}^{\infty}(\mathcal{S})$) local extension encodes the expectation that representations of high-dimensional data change smoothly with small perturbations in the data, and is satisfied when a representation is the minimizer of a smooth penalty function. Equivalence by nonvanishing functions in $C^{\infty}(\mathcal{S})$ allows us to regard different schemes of input weighting which optimize the same penalty function as constituting the same brain representation. The dissimilarity function δ_{φ} reflects the license to choose a measure of inter-subject variability that is popular (in the field) for a particular brain representation φ . Finally, we note that the ambient dimension d of the representation space varies widely in our problem context ($1 < \log_{10}(d) < 7$; see Table 2.1), but we always have $d \ll D$.

Given a collection of representations $\{\varphi_i : \widehat{\mathcal{S}} \rightarrow \mathbb{R}^{d_i}\}$, we wish to estimate topological differences between the spaces $\mathcal{S}_i := \tilde{\varphi}_i(\mathcal{S})$. Let $\widehat{\mathcal{S}}_i := (\varphi_i(\widehat{\mathcal{S}}), \delta_i)$ denote the finite metric space specified by φ_i and the dissimilarity function δ_i . When possible, choose an extension $\tilde{\varphi}_i$ for which \mathcal{S}_i is a smooth manifold admitting a Riemannian distance function that agrees with δ_i on $\widehat{\mathcal{S}}_i$; otherwise, construct a non-negative symmetric function on $\mathcal{S}_i \times \mathcal{S}_i$ that restricts to δ_i and pulls back to a smooth function on $\mathcal{S} \times \mathcal{S}$ by $\tilde{\varphi}_i$.

In this setting, we may view the Vietoris-Rips persistence²¹ of the finite metric spaces $\widehat{\mathcal{S}}_i$ as estimates of the topological features of the spaces \mathcal{S}_i ; we can then compute topological differences in the metric space of persistence diagrams.^{22,23}

2.1.1 Generalizing to unseen data

As a final note, we remark that it is not necessary to assume that all representation maps φ_i are learned on the same sample $\widehat{\mathcal{S}}$. If we assume that $\widehat{\mathcal{S}}$ and $\widehat{\mathcal{S}}'$ are independent uniform samples from \mathcal{S} (i.e., $\widehat{\mathcal{S}} \sim \widehat{\mathcal{S}}'$), then $\widehat{\mathcal{S}}_i$ and $\widehat{\mathcal{S}}'_i$ (asymptotically) generate the same approximation of the persistence of $\tilde{\varphi}_i(\mathcal{S})$. Relaxing the assumption that $\text{dom}(\varphi_i) = \widehat{\mathcal{S}}$ for all i , representation maps out of different datasets (provided they are sampled from similar populations) should produce similar topological information. By the same argument, topological differences between $\widehat{\mathcal{S}}_i$ and $\widehat{\mathcal{S}}'_i$ for some collection of representations $\{\varphi_i\}$ (e.g., a family of random projections) should robustly detect differences in the distribution of $\widehat{\mathcal{S}}$ and $\widehat{\mathcal{S}}'$, even when both distributions are high-dimensional.

Regarding the finite metric spaces $\widehat{\mathcal{S}}_i, \widehat{\mathcal{S}}_j$ as simple undirected graphs G_i, G_j with positive weights, we may, equivalently, state that our method does not require that the graphs share a vertex set, or even have the same number of vertices. We require only that the vertex sets V_i and V_j be sampled from similar distributions in the same space. This is a much weaker condition and allows our method to facilitate representations comparisons across a very broad class of datasets.

2.2 Topological data analysis

This section describes our use of TDA tools, namely Vietoris-Rips persistence²¹ and the topological bootstrap,^{1,13} to compute topological differences between data representations. First, we compute the Vietoris-Rips persistence²¹ of the finite metric spaces $\widehat{\mathcal{S}}_i$ induced by different brain representations (see Section 2.4) and choices of dissimilarity function (see Section 2.5). Next, we examine the re-sampling stability of the Vietoris-Rips persistence for each representation by computing a prevalence score from its topological bootstrap (Section 2.2.2). Finally, we use this prevalence score to compute a prevalence-weighted variant of the p -Wasserstein distance between different representations

(see Section 2.2.3), and perform Ward hierarchical clustering²⁴ in the ensuing pre-metric space of persistence diagrams.

2.2.1 Vietoris-Rips persistence

We begin with a brief primer on the Vietoris-Rips persistence. For a more thorough treatment of the Vietoris-Rips persistence, see Dey & Wang's text;²¹ see Hatcher's text²⁵ for a full treatment of homology and other algebraic topology preliminaries.

The topology of a space can be summarized by its *homology groups*, algebraic invariants that describe its structure. Persistent homology extends the constructions of homology to finite data, delivering a multiscale and threshold-free estimation of data topology. To compute the persistent homology of a dataset X , it must first be equipped with a *simplicial structure*: a simplicial complex $K(X)$ is a set of subsets of X with the property that $\sigma' \in K$ whenever $\sigma' \subset \sigma$ for some $\sigma \in K$, and a *filtration* is a collection $\{K_t(X)\}$ such that $K_s \subset K_t$ when $s < t$. Homology groups $H_k(K_t(X))$ of dimension k can be computed for each simplicial complex, and their *persistence* $\text{PH}_k(X)$ is described by the evolution of these groups across the filtration.

One important simplicial complex that can be placed on any finite metric space (X, δ) (equivalently, any simple undirected graph with positive weights) is the **Vietoris-Rips complex**, which we employ in this work. The Vietoris-Rips complex $\text{VR}_\rho(X, \delta)$ of radius ρ is defined as

$$\text{VR}_\rho(X, \delta) = \{S \subset X \mid \delta(x, x') \leq \rho \text{ for all } x, x' \in S\}.$$

When context is clear, we will drop δ from the notation and simply write $\text{VR}_\rho(X)$. Since $\text{VR}_\rho(X) \subset \text{VR}_{\rho'}(X)$ whenever $\rho < \rho'$, the collection $\text{VR}(X) := \{\text{VR}_\rho(X)\}_{\rho \geq 0}$ is a filtration called the **Vietoris-Rips filtration**. By inducing a Vietoris-Rips filtration, any dissimilarity function δ_X on a finite set X specifies its **Vietoris-Rips persistence** $\text{PH}(X) := \bigoplus_k \text{PH}_k(\text{VR}(X))$. In this work, we will use $\text{PH}(X)$ or $\text{PH}_k(X)$ to denote the Vietoris-Rips persistence of the finite metric space (X, δ) unless explicitly stated otherwise.

2.2.2 Topological bootstrap

We give a brief overview of topological bootstrapping¹³ in the following section.

Because it is possible (and, in fact, generic) for multiple data elements to define the same homology generator, bootstrap re-sampling²⁶ is less straightforward in persistent homology than in many other modes of analysis. However, Reani and Bobrowski recently demonstrated a "topological bootstrap" method¹³ that uses image persistence²² to register homology generators found in co-embeddable spaces. If X, Y can both be embedded into a shared space Z , then the inclusion maps $X \xrightarrow{\iota_X} Z$ and $Y \xrightarrow{\iota_Y} Z$ induce homology maps ι_X^*, ι_Y^* with corresponding filtration maps $\iota_{r,X}^*, \iota_{r,Y}^*$ (assuming compatible filtrations on each space).

A pair of nontrivial elements in $\text{PH}_k(X)$ and $\text{PH}_k(Y)$ is said to "match at r via Z " if $\iota_{r,X}^*$ and $\iota_{r,Y}^*$ map them to the same nontrivial element of $\text{PH}_k(Z)$ for some filtration value r . For a matched pair, the affinity score α of the match can be computed from ratios of lengths of filtration intervals for which elements in $\text{PH}_k(X)$ and $\text{PH}_k(Y)$ are matched via Z . We assign $\alpha = 0$ when no match is found and have $\alpha \in (0, 1]$ otherwise.

This procedure simplifies substantially in the bootstrapping case; we then have $Z = X$ and $Y = \widehat{X} \subset X$, and we need only check nontrivial elements of $\text{PH}_k(X)$ for matches in $\text{PH}_k(\widehat{X})$. In the bootstrap setting, Reani and Bobrowski measure the re-sampling stability of a nontrivial generator $\gamma \in \text{PH}_k(X)$ by its *prevalence score*

$$\rho(\gamma) := \frac{1}{R} \sum_{j=1}^R \alpha(\gamma, \widehat{\gamma}_j), \quad (2.1)$$

where $\widehat{\gamma}_j$ is the match of γ in the j^{th} bootstrap \widehat{X}_j . This is just the average affinity (over all bootstraps) between γ and its matches. In the present study, we compute prevalence scores for each generator in $\text{PH}_1(X)$.

The specific challenges of our problem context required a mild extension of existing topological bootstrapping implementations. Our implementation²⁷ of the topological bootstrap builds on Garcia-

Redondo et al’s work,¹⁴ which efficiently integrates cycle registration with Ripser²⁸ and Ripser-image²⁹ and refines the cycle affinity measures proposed by Reani and Bobrowski. We extend their implementation by broadening the conditions under which topological bootstrapping may be applied to include the case of arbitrary, precomputed metrics.

We conducted cycle registration using $R = 1000$ bootstraps per dataset at 90% re-sampling (without replacement), and we consider $k = 1$ -dimensional cycle registration in this work.

2.2.3 Prevalence-weighted p -Wasserstein

The space of persistence diagrams is a metric space²³ under the p -Wasserstein distance, which previous work⁸ has used to compare persistence diagrams of different reduced-dimension data representations. We also wish to include information about the re-sampling stability of the persistence when comparing persistence diagrams. To do so, we define the *prevalence-weighted p -Wasserstein* as

$$W_p^{(\rho)} \left(\text{PD}_X^{(k)}, \text{PD}_Y^{(k)} \right) := \inf_{\phi \in \Gamma_{XY}} \left(\sum_{\gamma \in \text{PD}_X^{(k)}} |\rho_X(\gamma) - \rho_Y(\phi(\gamma))|^p \|\gamma - \phi(\gamma)\|_p^p \right)^{\frac{1}{p}} \quad (2.2)$$

Here, $\text{PD}_X^{(k)}$ and $\text{PD}_Y^{(k)}$ are k -persistence diagrams, and Γ_{XY} is the set of bijections between PD_X and PD_Y , while $\rho_X(x)$ and $\rho_Y(\phi(x))$ are the homology generator prevalence scores defined by Equation (2.1) over, respectively, subsamples of X and Y . This is a simple re-weighting of the usual Wasserstein distance, modified to incorporate the prevalence score as a summary of per-cycle stability statistics. Note that generators with a prevalence of 0 have a distance of 0 from the diagram diagonal: a nontrivial cycle that fails matching in every bootstrap is trivialized by $W_p^{(\rho)}$. The theorem below asserts that the trivialization of unstable cycles is the primary point of departure of $W_p^{(\rho)}$ from W_p , the typical p -Wasserstein distance, with which it otherwise shares important desirable properties.

Theorem 1. Suppose $\text{PH}_k(X)$ and $\text{PH}_k(Y)$ are k -persistence modules, each equipped with a weighting function $\tilde{\rho}_* : \text{PH}_k(*) \rightarrow [0, 1]$. If $\text{PD}_X^{(k)}$ and $\text{PD}_Y^{(k)}$ are the respective diagrams of $\text{PH}_k(X)$ and $\text{PH}_k(Y)$, then the dissimilarity function $W_p^{(\rho)}$ given by Equation (2.2) is bounded above by the p -Wasserstein distance and is a pre-metric on the space \mathcal{PD} of persistence diagrams.

The theorem above follows almost immediately from the symmetry and nonnegativity of the Wasserstein distance, along with the fact that prevalence scores lie in the unit interval. However, we include the proof in Appendix A.1 for completeness. One important corollary of the theorem above is that $(\mathcal{PD}, W_p^{(\rho)})$ inherits perturbation stability from (\mathcal{PD}, W_p) .²³

2.2.4 The Matched Betti Number

We also define the " k^{th} matched Betti number" $\beta_k^{(\text{matched})}(X, \delta)$ as the number of matched cycles (i.e., matches with nonzero affinity scores) found in each bootstrapped re-sample \hat{X}_j . Intuitively, this is a count of the number of stable generators found in each bootstrap. The Betti numbers of a persistence module are typically summarized by curves, since each value of a filtration may induce a homology with a different set of Betti numbers. However, since the topological bootstrap already uses persistence interval information to find matched cycles and compute their affinity, we may consider $\beta_k^{(\text{matched})}$ as having "collapsed" these curves via cycle registration. We view the distribution of bootstrapped $\beta_k^{(\text{matched})}$ values as a coarse summary of the stability of the distributed persistence^{19,20} of a finite metric space (X, δ) .

2.3 Dataset

The data for this study consists of pre-processed resting-state functional MRI data from $N = 1003$ Human Connectome Project young adult (HCP-YA)³⁰ subjects. HCP-YA resting state fMRI data were acquired on a 3T Siemens scanner using the HCP protocol ($TR = 0.72$ sec, $TE = 33$ ms, isotropic voxel size = 2mm, multiband factor 8). After pre-processing, each subject’s data consists of a matrix of 91,282 “grayordinates” (a fixed atlas of graph vertices on the surface of the brain), with

1200 time samples at each grayordinate. We treat this as our pre-representation source data, giving an embedding dimension of $D = 91282 \times 1200 \sim 10^8$ in the initial space.

The HCP-YA dataset also contains a rich family structure, including 149 genetically confirmed monozygotic twin pairs and 94 genetically confirmed dizygotic twin pairs, non-twin siblings and half-siblings, and parents. Family structure in the HCP-YA dataset creates invalidates simple re-sampling as a viable bootstrap approach, since data are not exchangeable. To properly account for this family structure while bootstrapping, we followed the approach of Winkler et al.³¹ and excluded all bootstrap re-samples that placed individuals with the same mother on different sides of the inclusion/exclusion divide.

2.4 Brain Representations

The brain representations we consider can roughly be grouped by their underlying models of brain function. We characterize the first group of methods as seeking to cluster neural activity into spatially contiguous cortical “parcels.” In the parcellation family, we have Yeo’s parcellated networks,³² Glasser’s multimodal parcellation,³³ and Schaefer’s local-global parcellation.³⁴ We also sample from a family of low-rank matrix factorization methods that parse non-contiguous networks of functional activity. Independent component analysis (ICA),³⁵ a generalization of PCA, underlies perhaps the most widely used brain representation in the field³⁶ and thus is represented here. In addition, we consider PROFUMO,³⁷ which parses “functional modes” of brain activity from hierarchical Bayesian signal models. Finally, we include the “principal gradient” (or “gradients”),³⁸ a diffusion embedding method that organizes brain function through cortical geometry. The parcellation methods have fixed representation parameters. For the others, we vary the decomposition rank parameter over a representative set of values (see Table 2.1).

From each brain representation, one or more feature types were computed to reflect the typical use of brain representations in the neuroimaging literature. The five feature types considered in this work are as follows: (1) “amplitude,” the average power of the time signal in a given spatial component; (2) “network matrix (netmat),” the matrix of pairwise Pearson similarities of time courses for each pair of spatial components; (3) “partial correlation,” the variance-normalized precision matrix; (4) “map,” the spatial membership weights of a given spatial component in grayordinate space; and (5) “spatial network matrix”, the matrix of pairwise Pearson similarities of maps for each spatial component. The decomposition rank, feature types, and number of features for each brain representation is summarized in Table 2.1. Note that since subject data are encoded in terms of features, it is the feature number and **not** the brain representation’s decomposition rank that denotes the dimension d of the target embedding space in the mapping $\hat{\varphi} : \hat{S} \rightarrow \mathbb{R}^d$. We compare subject-space embeddings using the pairwise dissimilarities of their points, which we compute as described in the next section.

Representation	Rank(s) r	Considered Feature Type(s)	Feature Number(s) d
PROFUMO	33	maps, spatial network matrices	$91282 \times 33, \binom{33}{2}$
Dual-regression spatial ICA	15, 25, 50, 100, 200, 300	amplitudes, network matrices, partial network matrices	$r, \binom{r}{2}, \binom{r}{2}$
Glasser parcellation	360	amplitudes, network matrices, partial network matrices	$360, \binom{360}{2}, \binom{360}{2}$
Schaefer parcellation	100, 200, 300, 600, 1000	amplitudes, network matrices, partial network matrices	$r, \binom{r}{2}, \binom{r}{2}$
Yeo parcellation	17	amplitudes, network matrices, partial network matrices	$17, \binom{17}{2}, \binom{17}{2}$
Gradient (diffusion embedding)	1, 15, 25, 50, 100, 200, 300	maps	$91282 \times r$

Table 2.1: The combinations of brain representation, decomposition rank parameters, and feature types investigated in the present work.

2.5 Dissimilarity functions

For each brain representation method, decomposition rank within a given representation, and considered feature type, we compute pairwise distances between all subjects. Each feature type under

consideration is structured either as a vector (maps, amplitudes) or a symmetric positive semidefinite (SPSD) matrix (network matrices). This bifurcation of data types is echoed in our choice of measures when computing the dissimilarity between a pair of subjects. In both the vector case and the SPSPD data case, we ran our analysis using one dissimilarity function intrinsic to the data type and another derived from the Pearson correlation. We use Pearson-based dissimilarities in deference to the ubiquitous use of the Pearson correlation in neuroimaging analyses.

We now define the dissimilarity functions we use on vector data. Suppose s_i and s_j are data vectors in \mathbb{R}^d , and let $\rho(s_i, s_j)$ denote their Pearson correlation. Let $\langle \cdot, \cdot \rangle$ denote the usual inner product on \mathbb{R}^d . We then define

$$\delta_{v_1}(s_i, s_j) = 1 - \langle s_i, s_j \rangle^2 \quad (2.3)$$

$$\delta_{v_2}(s_i, s_j) = 1 - \rho^2(s_i, s_j), \quad (2.4)$$

assuming the matrix $\delta_{ij} = \langle s_i, s_j \rangle$ is scaled to have entries in $[0, 1]$. Note that we can interpret δ_{v_2} as approximately the angular distance between the vectors s_i and s_j after each has been centered. We refer to δ_{v_1} as the "inner product divergence" and δ_{v_2} as the "Pearson divergence".

In the SPSPD matrix case, we consider the geodesic distance between matrices on the Riemannian SPD cone³⁹ alongside a (modified) Pearson divergence. The geodesic distance δ_{pd_1} on the symmetric positive definite cone,⁴⁰ given by

$$\delta_{pd_1}(A_i, A_j) = \|\log(A_i^{-1}A_j)\|_F \quad (2.5)$$

is efficiently implemented via the approximate joint diagonalizer,⁴¹ and we modify the Pearson divergence δ_{v_2} for the correlation matrix case by precomposing it with Fisher's z-transformation⁴² (the inverse hyperbolic tangent function). We write

$$\delta_{pd_2}(A_i, A_j) = \operatorname{atanh}^* \delta_{v_2}(\hat{a}_i, \hat{a}_j), \quad (2.6)$$

where \hat{a}_i is the half-vectorization of the symmetric matrix A_i (diagonal excluded). This precomposition is necessary for correlation matrices, as it normalizes the correlation values before re-correlating them. In contrast to the vector case, there is no simple comparison to be made between these two dissimilarity functions.

For each combination of brain representation, rank parameter, and feature type shown in Table 2.1, we compute pairwise dissimilarity according to both of whichever two measures are relevant. The subject-pairwise matrix of dissimilarities then forms the Gram matrix used to compute the persistent homology, as we describe in the next section.

2.6 Study Design

In Table 2.1, we lay out parameter and feature selections considered for each brain representation. For every representation, bootstrapped persistence is computed for all combinations of feature, parameter, and dissimilarity function considered; this gives a total of 90 subject-pairwise dissimilarity matrices for which we compute $R = 1000$ topological bootstraps. We compute the prevalence-weighted Wasserstein-2 distance between all pairs of methods and the $\beta_1^{\text{(matched)}}$ distributions for each method. This method-pairwise distance matrix then undergoes Ward hierarchical clustering²⁴ to determine similarity. Our code is publicly available on github.⁴³

2.6.1 Hypotheses

Comparing across feature and metric choices, we expect the SPD matrix geodesic distance to exhibit less sensitivity to concentration of measure and thus provide greater distinction between brain representations. We expect that within-feature groupings for map and amplitude will differ very little between the considered vector dissimilarity functions (equations 2.3 and 2.4). For all comparisons, we expect feature number and type to be more important drivers of differences than decomposition rank. Finally, within the PROFUMO analysis, we expect that spatial network matrices will be further from null than spatial maps, where we expect the very high dimensions of the spatial maps to suffer from concentration of measure.

Comparing across different brain representations, we expect to primarily see clustering according to (approximate) feature number and type, with secondary similarity clusters forming within each given

brain representation. We expect our analysis to align with previous results in the literature linking shared variance in brain representations,^{15,16,44,45} the details of which we expand upon in the results below.

3 Results

3.1 Triviality of persistence structure in some representation types

We first note several unexpected instances of trivial (or nearly trivial) persistence structure. First, full correlation matrices generated null H_1 persistence at every decomposition rank in every brain representation, irrespective of dissimilarity function choice. By contrast, the partial correlation matrices (similar by conjugation to the inverse of the full correlation matrix) have nontrivial persistence for nearly all feature types, decomposition ranks, and dissimilarity functions. Additionally, the inner product divergence (2.3) generated trivial or almost trivial homology in both maps and amplitudes, across all ranks and representations; this is not true of the Pearson divergence, which we incorrectly hypothesized would exhibit similar behavior. A complete tree of all methodological choices that exhibited trivial H_1 persistence is given in Figure B.5.

3.2 Effect of embedding dimension

Our analysis saw that topological complexity (as measured by H_1 persistence) generally *decreased* with the number of features considered (Figure B.1). Under the geodesic distance, mean prevalence score increased with feature number; for all other dissimilarity functions, mean prevalence score was not correlated with feature number (Figure B.2). Taken together, these observations suggest that embeddings in higher dimensions elicit a smaller number of nontrivial H_1 generators which are also more robust. This runs counter to the consequences we might expect from concentration of measure in high dimensions, which pushes spaces towards the discrete topology (and thus a higher number of less stable generators). As expected, we also saw that feature number was a more important driver of persistence structure than the underlying rank of the decomposition (Figure B.3).

3.3 Persistence vs. prevalence

We see evidence further corroborating Reani and Bobrowski’s observation that the most prevalent cycles are not always the most persistent ones.¹³ Figure 3.1 shows a sample persistence diagram in H_1 (colored by generator prevalence score) and a plot of all persistence-prevalence pairs observed in this experiment. Both plots demonstrate that cycles with low persistence can still have high prevalence, suggesting that the topological "noise" may carry meaningful structure in our data. In addition, we see a substantially richer difference structure between target embeddings when using the prevalence-weighted Wasserstein instead of the typical Wasserstein distance (Figure B.4).

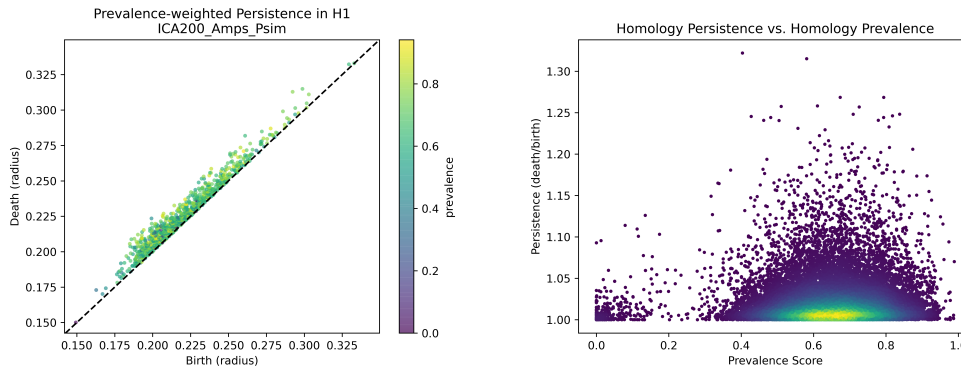


Figure 3.1: **(Left)** A sample persistence diagram, with color weights given by prevalence score. **(Right)** Persistence versus prevalence across all data collected, colored with a Gaussian kernel density estimator.

3.4 Persistence differences of brain representations

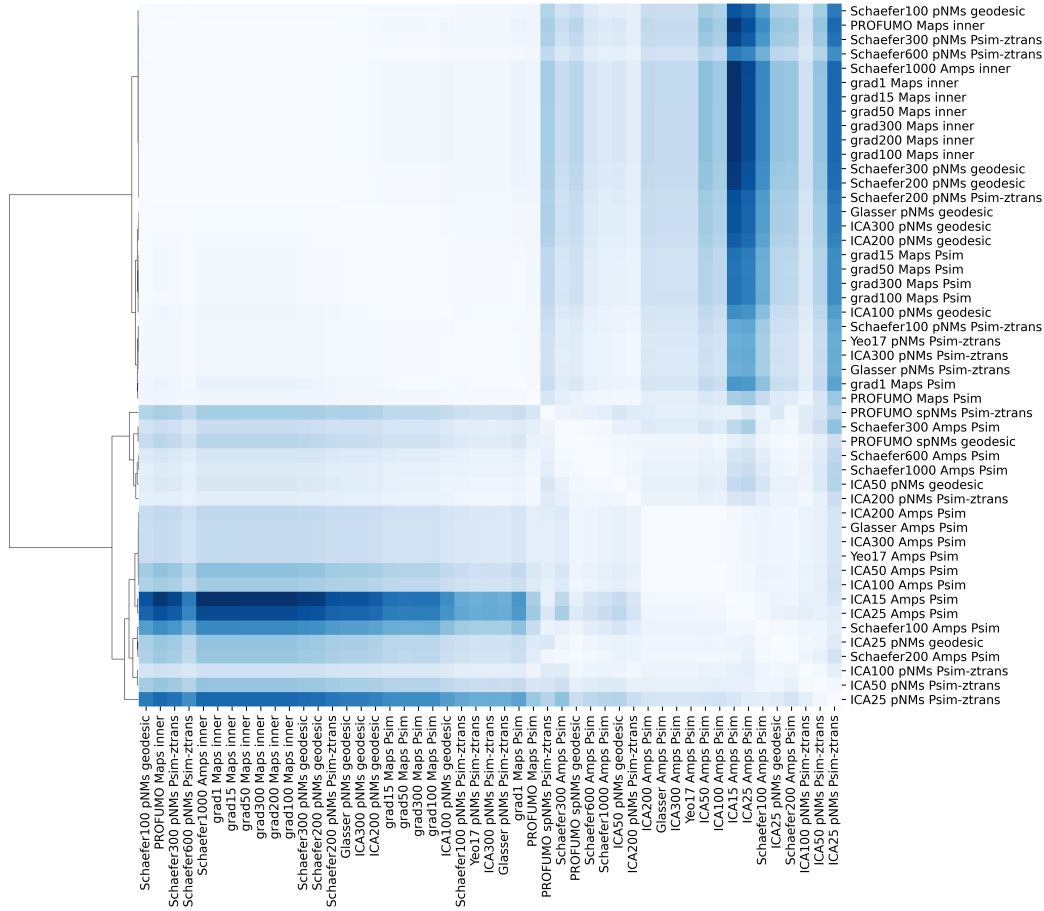


Figure 3.2: Prevalence-weighted 2-Wasserstien distances between H_1 persistence diagrams for all pairs of methods combinations with nontrivial first homology. Ward hierarchical clustering gives the dendrogram on the left side of the plot, which organizes labels into groups that maximally share variance. Lighter colors denote smaller distances, while darker (blue) colors denote larger ones.

The prevalence-weighted Wasserstein distance makes its strongest distinction between amplitudes and network matrix/spatial map feature types, which form the two main diagonal blocks and highest dendrogram branches (Fig 3.2). As hypothesized, this implies that our method distinguishes more strongly between feature type (and number) than between brain representation type, which forms the next set of blocks and branches. This is still somewhat surprising, however, because brain representations differ substantially in terms of whether they are unilateral or bilateral, binary or weighted, and decomposition rank.

We are also surprised to see PROFUMO spatial network matrices in the amplitude block. Both amplitudes⁴⁶ and spatial network matrices⁴⁷ have been shown to be highly sensitive to individual differences in behavior, but these feature types are interpreted very differently. Amplitudes may be linked to within-network synchronization,⁴⁸ within-network plasticity,⁴⁹ or within-network interneuron function,⁵⁰ whereas spatial network matrices are indicative of between-network shared brain regions that may play a role in cross-network integration.⁴⁷ Both amplitudes and spatial netmats have higher test-retest reliability (i.e., within-subject stability) than the features in the other block.^{37,51} Given this context, the clustered blocks of the prevalence-weighted Wasserstein may constitute a segregation of trait-sensitive (amplitude and spatial network matrix) from state-sensitive (temporal network matrix) features. This observation highlights the need for an evaluation method that can detect *which* elements of the persistence module are shared across representations, rather than only being able to similar topologies of subject similarity.

3.5 Computational resources

All other computations, including cycle registration, were negligible in cost compared to the computation of persistence modules for all bootstraps — roughly 270,000 persistence modules were computed in total. Memory demands remained relatively low ($\leq 50\text{GB}$ per homology computation). Our implementation was embarrassingly parallel on a queue-managed HPC cluster. We estimate that this experiment used approximately 80,000 CPU hours over the course of a month. Computation of image-persistence was the most costly individual step, with each embedded persistence module taking 1-3 hours to compute (compared to order of 10 minutes or less for other persistence computations).

4 Discussion

4.1 Conclusions

Our method reveals interesting relationships between representations of resting-state fMRI data. The prevalence-weighted Wasserstein distance distinguishes much more strongly between feature type than parcellation choice, potentially segregating trait-sensitive from state-sensitive features. Notably, this claim holds irrespective of our choice(s) of dissimilarity function.

Without exception, full network matrices gave rise to trivial PH_1 modules. Persistence modules generated from the inner product divergence (2.3) were (approximately) trivial as well, in sharp contrast to those generated from the Pearson divergence (2.4); this suggests that amplitude and spatial map features of brain representations tend to be "mean-dominated," in the sense that per-subject deviations from group-level structures are typically small.

In addition, we saw a counterintuitive decrease in persistence "complexity" as a function of increasing embedding dimension, which highlights the difficulties of evaluating high-dimensional representations of data from very high-dimensional source spaces. We also examined the relationship between persistence and prevalence, finding that the two are largely uncorrelated for our data. Coupled with the stronger distinctions realized by the prevalence-weighted Wasserstein, we believe that persistence and prevalence carry complementary information as measures of cycle importance. We also characterized a few key properties of the prevalence-weighted Wasserstein: namely, it is a pre-metric that inherits perturbation stability from W_p .

4.2 Limitations

Because of the high cost of parameter exploration, parcellation computation, and topological bootstrapping, only a few representation methods were examined in this work. An extension of this analysis to a wider array of brain representations may be warranted, especially newer methods that derive an explicitly geometric basis for functional activity (e.g., Laplacian eigenvalues⁵²).

Another important limitation of our work is the very high dimension-to-sample-size ratio ($N \ll d$) of our data. In this regime, it is difficult to ascertain what features we see because of structure in the data and what topological features are products of the curse of dimensionality. This could be partially ameliorated by conducting our analysis over adequately constructed null data and comparing the results, which is beyond the scope of this work.

4.3 Future Directions

In addition to addressing some of the limitations noted above, we offer several directions for follow-up work on this study. First, we propose a consideration of the per-bootstrap Wasserstein distance between methods; a distributional picture of differences in the endogenous metric of persistence modules could yield important insights. Second, it is possible to repurpose the topological bootstrap to track the addition/deletion of homology components by different brain representation; practically, this is primarily hindered by the lack of a suitable dissimilarity function between pairs of points under different embeddings. Finding and validating such a metric would be a valuable direction of inquiry. Finally, we wish to suggest a deeper characterization of the theoretical properties of the prevalence-weighted Wasserstein and its relationship to distributed persistence.

References

- [1] Gracia, A., González, S., Robles, V. & Menasalvas, E. A methodology to compare dimensionality reduction algorithms in terms of loss of quality. *Inf. Sci. (Ny)* **270**, 1–27 (2014).
- [2] Lee, J. A. & Verleysen, M. Quality assessment of dimensionality reduction: Rank-based criteria. *Neurocomputing* **72**, 1431–1443 (2009).
- [3] Lee, J. A. & Verleysen, M. Two key properties of dimensionality reduction methods. In *2014 IEEE Symposium on Computational Intelligence and Data Mining (CIDM)* (IEEE, 2014).
- [4] Wang, Y., Huang, H., Rudin, C. & Shaposhnik, Y. Understanding how dimension reduction tools work: an empirical approach to deciphering t-SNE, UMAP, TriMap, and PaCMAP for data visualization. *The Journal of Machine Learning Research* **22**, 201:9129–201:9201 (2022).
- [5] Amari, S.-i. *Information Geometry and its Applications*, vol. Volume 194 (2016). URL <http://www.springer.com/series/34>.
- [6] Tyagi, H., Vural, E. & Frossard, P. Tangent space estimation for smooth embeddings of riemannian manifolds. *information and inference: A. Journal of the IMA* **2**, 69–114 (2013).
- [7] Singer, A. & Wu, H.-T. Vector diffusion maps and the connection laplacian. *Commun. Pure Appl. Math.* **65**, 1067–1144 (2012).
- [8] Rieck, B. & Leitte, H. Persistent homology for the evaluation of dimensionality reduction schemes. *Comput. Graph. Forum* **34**, 431–440 (2015).
- [9] Paul, R. & Chalup, S. K. A study on validating non-linear dimensionality reduction using persistent homology. *Pattern Recognit. Lett.* **100**, 160–166 (2017).
- [10] Barannikov, S., Trofimov, I., Balabin, N. & Burnaev, E. Representation Topology Divergence: A Method for Comparing Neural Network Representations (2022). URL <http://arxiv.org/abs/2201.00058>. ArXiv:2201.00058 [cs, math].
- [11] Fasy, B. T. & Qin, Y. *Comparing Distance Metrics on Vectorized Persistence Summaries* (2020).
- [12] Berry, E., Chen, Y.-C., Cisewski-Kehe, J. & Fasy, B. T. Functional summaries of persistence diagrams. *J. Appl. Comput. Topol.* **4**, 211–262 (2020).
- [13] Reani, Y. & Bobrowski, O. Cycle registration in persistent homology with applications in topological bootstrap (2021).
- [14] García-Redondo, I., Monod, A. & Song, A. Fast topological signal identification and persistent cohomological cycle matching (2022).
- [15] Dadi, K. *et al.* Benchmarking functional connectome-based predictive models for resting-state fMRI. *NeuroImage* **192**, 115–134 (2019). Publisher: Academic Press Inc.
- [16] Botvinik-Nezer, R. *et al.* Variability in the analysis of a single neuroimaging dataset by many teams. *Nature* **582**, 84–88 (2020). URL <https://doi.org/10.18112/openneuro>. Publisher: Nature Research.
- [17] Bijsterbosch, J. *et al.* Challenges and future directions for representations of functional brain organization. *Nat. Neurosci.* **23**, 1484–1495 (2020).
- [18] Trofimov, I. *et al.* Learning Topology-Preserving Data Representations (2023). URL <http://arxiv.org/abs/2302.00136>. ArXiv:2302.00136 [cs, math].
- [19] Bubenik, P., Hull, M., Patel, D. & Whittle, B. Persistent homology detects curvature. *Inverse Probl.* **36**, 025008 (2020).
- [20] Solomon, E., Wagner, A. & Bendich, P. From geometry to topology: Inverse theorems for distributed persistence (2021). 2101.12288.
- [21] Dey, T. K. & Wang, Y. *Computational topology for data analysis* (Cambridge University Press, Cambridge, England, 2022).
- [22] Cohen-Steiner, D., Edelsbrunner, H., Harer, J. & Morozov, D. Persistent homology for kernels, images, and cokernels. In *Proceedings of the Twentieth Annual ACM-SIAM Symposium on Discrete Algorithms*, 1011–1020 (Society for Industrial and Applied Mathematics, Philadelphia, PA, 2009).
- [23] Skraba, P. & Turner, K. Wasserstein Stability for Persistence Diagrams. *arXiv:2006.16824 [math]* (2021). URL <http://arxiv.org/abs/2006.16824>. ArXiv: 2006.16824.

- [24] Ward, J. H., Jr. Hierarchical grouping to optimize an objective function. *J. Am. Stat. Assoc.* **58**, 236–244 (1963).
- [25] Hatcher, A. *Algebraic Topology* (Cambridge University Press, 2002).
- [26] Abu-Mostafa, Y. S., Magdon-Ismail, M. & Lin, H.-T. *Learning from Data* (2012).
- [27] Easley, T. Fork from inesgare/interval-matching. https://github.com/tyo8/interval-matching_bootstrap. Accessed: 2023-9-28.
- [28] Bauer, U. Ripser: efficient computation of Vietoris–Rips persistence barcodes. *J. Appl. Comput. Topol.* **5**, 391–423 (2021).
- [29] Bauer, U. & Schmah, M. Efficient computation of image persistence (2022).
- [30] Glasser, M. F. *et al.* The human connectome project’s neuroimaging approach. *Nat. Neurosci.* **19**, 1175–1187 (2016).
- [31] Winkler, A. M., Webster, M. A., Vidaurre, D., Nichols, T. E. & Smith, S. M. Multi-level block permutation. *Neuroimage* **123**, 253–268 (2015). URL <https://www.ncbi.nlm.nih.gov/pmc/articles/PMC4644991/>.
- [32] Yeo, B. T. T. *et al.* The organization of the human cerebral cortex estimated by intrinsic functional connectivity. *J. Neurophysiol.* **106**, 1125–1165 (2011).
- [33] Glasser, M. F. *et al.* A multi-modal parcellation of human cerebral cortex. *Nature* **536**, 171–178 (2016). URL <https://www.nature.com/articles/nature18933>. Number: 7615 Publisher: Nature Publishing Group.
- [34] Schaefer, A. *et al.* Local-global parcellation of the human cerebral cortex from intrinsic functional connectivity MRI. *Cereb. Cortex* **28**, 3095–3114 (2018).
- [35] Comon, P. Independent component analysis, a new concept? *Signal Processing* **36**, 287–314 (1994).
- [36] Nickerson, L. D., Smith, S. M., Öngür, D. & Beckmann, C. F. Using dual regression to investigate network shape and amplitude in functional connectivity analyses. *Front. Neurosci.* **11**, 115 (2017).
- [37] Harrison, S. J. *et al.* Modelling subject variability in the spatial and temporal characteristics of functional modes. *Neuroimage* **222**, 117226 (2020).
- [38] Margulies, D. S. *et al.* Situating the default-mode network along a principal gradient of macroscale cortical organization. *Proc. Natl. Acad. Sci. U. S. A.* **113**, 12574–12579 (2016).
- [39] Moakher, M. A differential geometric approach to the geometric mean of symmetric positive-definite matrices. *SIAM J. Matrix Anal. Appl.* **26**, 735–747 (2005).
- [40] Pennec, X., Fillard, P. & Ayache, N. A riemannian framework for tensor computing. *Int. J. Comput. Vis.* **66**, 41–66 (2006).
- [41] Congedo, M., Afsari, B., Barachant, A. & Moakher, M. Approximate joint diagonalization and geometric mean of symmetric positive definite matrices (2015). 1505.07343.
- [42] Fisher, R. A. Frequency distribution of the values of the correlation coefficient in samples from an indefinitely large population. *Biometrika* **10**, 507 (1915).
- [43] Easley, T. Persistent homology and brain representations repository. https://github.com/tyo8/brain_representations. Accessed: 2023-9-28.
- [44] Bijsterbosch, J. D. *et al.* The relationship between spatial configuration and functional connectivity of brain regions. *eLife* (2018). URL <https://doi.org/10.7554/eLife.32992.001>.
- [45] R, K. *et al.* Comparison Between Gradients and Parcellations for Functional Connectivity Prediction of Behavior. *Neuroimage* 120044 (2023). URL <https://www.win.ox.ac.uk/publications/1335479>.
- [46] Miller, K. L. *et al.* Multimodal population brain imaging in the UK Biobank prospective epidemiological study. *Nature Neuroscience* **19**, 1523–1536 (2016). URL <https://www.nature.com/articles/nn.4393>. Number: 11 Publisher: Nature Publishing Group.
- [47] Bijsterbosch, J. D., Beckmann, C. F., Woolrich, M. W., Smith, S. M. & Harrison, S. J. The relationship between spatial configuration and functional connectivity of brain regions revisited. *eLife* (2019).

- [48] Lee, S. *et al.* Amplitudes of resting-state functional networks - investigation into their correlates and biophysical properties. *NeuroImage* **265**, 119779 (2023).
- [49] Sydnor, V. J. *et al.* Intrinsic activity development unfolds along a sensorimotor–association cortical axis in youth. *Nature Neuroscience* **26**, 638–649 (2023). URL <https://www.nature.com/articles/s41593-023-01282-y>. Number: 4 Publisher: Nature Publishing Group.
- [50] Anderson, K. M. *et al.* Convergent molecular, cellular, and cortical neuroimaging signatures of major depressive disorder. *Proceedings of the National Academy of Sciences* **117**, 25138–25149 (2020). URL <https://www.pnas.org/doi/full/10.1073/pnas.2008004117>. Publisher: Proceedings of the National Academy of Sciences.
- [51] Dutt, R. K. *et al.* Mental health in the UK Biobank: A roadmap to self-report measures and neuroimaging correlates. *Human Brain Mapping* **43**, 816–832 (2022). URL <https://onlinelibrary.wiley.com/doi/abs/10.1002/hbm.25690>. _eprint: <https://onlinelibrary.wiley.com/doi/pdf/10.1002/hbm.25690>.
- [52] Pang, J. C. *et al.* Geometric constraints on human brain function (2023). URL <https://www.biorxiv.org/content/10.1101/2022.10.04.510897v2>. Pages: 2022.10.04.510897 Section: New Results.

A Appendix

A.1 Properties of the prevalence-weighted Wasserstein

For the purposes of the work in this manuscript, we are mainly concerned with checking that (a) $W_p^{(\rho)}$ has reasonable properties as a dissimilarity measure (we show it is a pre-metric) and (b) that it inherits diagram stability from W_p . These properties of the prevalence-weighted Wasserstein follow almost immediately from the definition, but we include the proof for completeness.

Theorem. Suppose $\text{PH}_k(X)$ and $\text{PH}_k(Y)$ are finitely generated k -persistence modules, each equipped with the weighting function $\tilde{\rho}_* : \text{PH}_k(*) \rightarrow [0, 1]$ defined by Equation 2.1. Let $\text{PD}_X^{(k)}, \text{PD}_Y^{(k)}$ denote the respective diagrams of $\text{PH}_k(X)$ and $\text{PH}_k(Y)$, and let Δ denote the diagonal (empty) diagram. With $W_p^{(\rho)}$ defined by Equation 2.2, we have

$$W_p^{(\rho)} \leq W_p,$$

where W_p is the usual Wasserstein distance. Furthermore,

1. $W_p^{(\rho)}(\text{PD}_X^{(k)}, \text{PD}_Y^{(k)}) \geq 0$, and $W_p^{(\rho)}(\text{PD}_0, \Delta) = 0$ for any sample-degenerate diagram PD_0 (see Definition A.1)
2. $W_p^{(\rho)}(\text{PD}_X^{(k)}, \text{PD}_Y^{(k)}) = W_p^{(\rho)}(\text{PD}_Y^{(k)}, \text{PD}_X^{(k)})$

Proof. The inequality $W_p^{(\rho)} \leq W_p$ follows immediately from the fact that ρ_X, ρ_Y take image in $[0, 1]$. Additionally, non-negativity and symmetry follow immediately from the corresponding properties of the absolute value and p -Wasserstein distance. If PD_0 is sample-degenerate, then $\rho_0(\gamma) = 0$ for every $\gamma \in \text{PD}_0$ by definition (A.1); it follows that $W_p^{(\rho)}(\text{PD}_0, \Delta) = 0$. \square

Definition A.1 (Sample-degenerate persistence interval). Suppose X is a finite measure space with k -persistence module $\text{PH}_k(X)$ and subsamples X_1, \dots, X_n defining a prevalence score $\rho : \text{PH}_k(X) \rightarrow [0, 1]$ on $\text{PH}_k(X)$ by Equation 2.1. Take a (possibly trivial) persistence interval $b \in \text{PH}_k(X)$; we say b is **sample-degenerate** if $\rho(b) = 0$. If a k -persistence diagram $\text{PD}_X^{(k)}$ descends from a module composed only of sample-degenerate intervals, we call it a **sample-degenerate diagram**.

B Supplementary figures

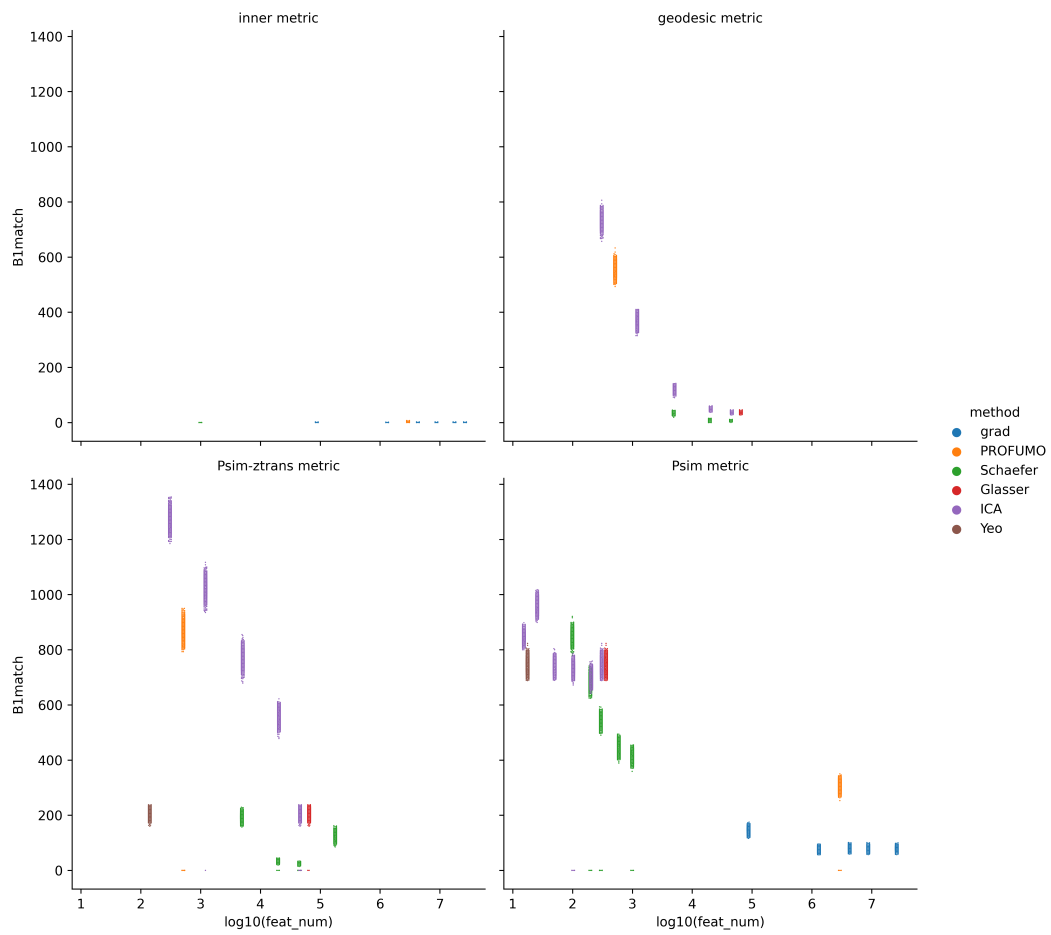


Figure B.1: Number of matched cycles as a function of feature number, separated by brain representation type, feature, and dissimilarity metric. PROFUMO features are spatial netmats for geodesic and z -transformed Pearson measures and maps otherwise. Diffusion gradient features are maps. All other features are either partial netmats (under geodesic or z -transformed Pearson measures) or amplitudes (under Pearson or inner product divergence).

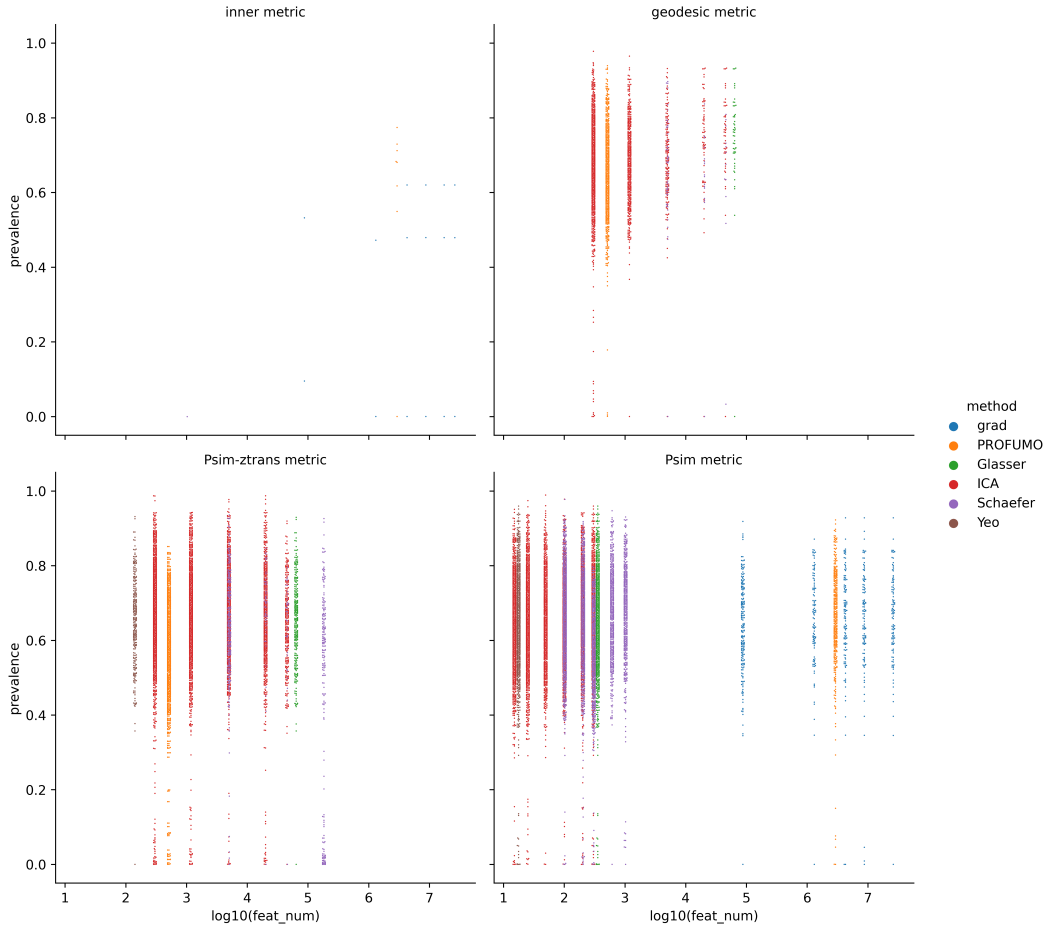


Figure B.2: The distribution of prevalence scores (average match affinity over bootstraps) does not vary with feature number, except under the geodesic distance. For partial and spatial network matrices under the geodesic distance, we see that generator sparsity and generator stability both *increase* as a function of feature number.

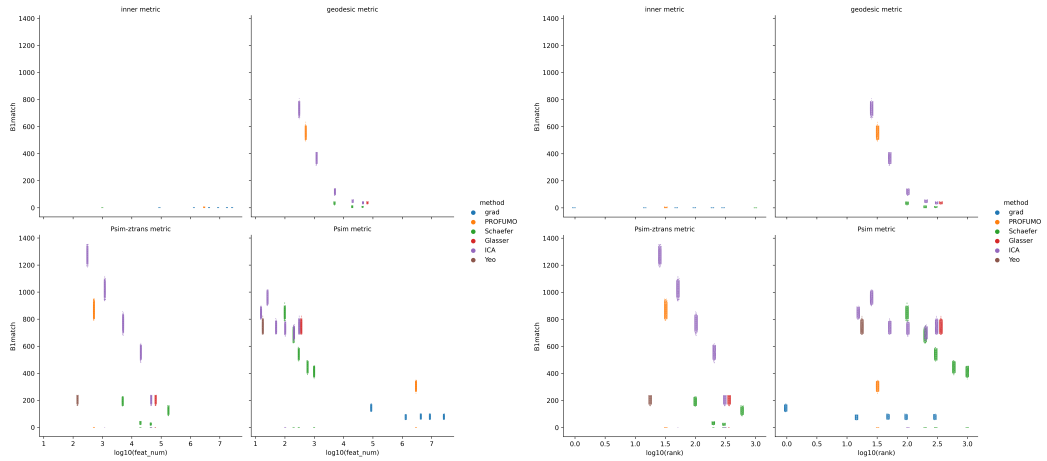


Figure B.3: The distribution of numbers of matched cycles, as a function of both feature number (**Left**)/Figure B.1 and decomposition rank (**Right**). We observe approximate monotonicity as a function of feature number, but not as a function of decomposition rank, suggesting that feature number is a more important driver of persistence structure than decomposition rank.

Wasserstein Dist. from
H1 persistence diagrams

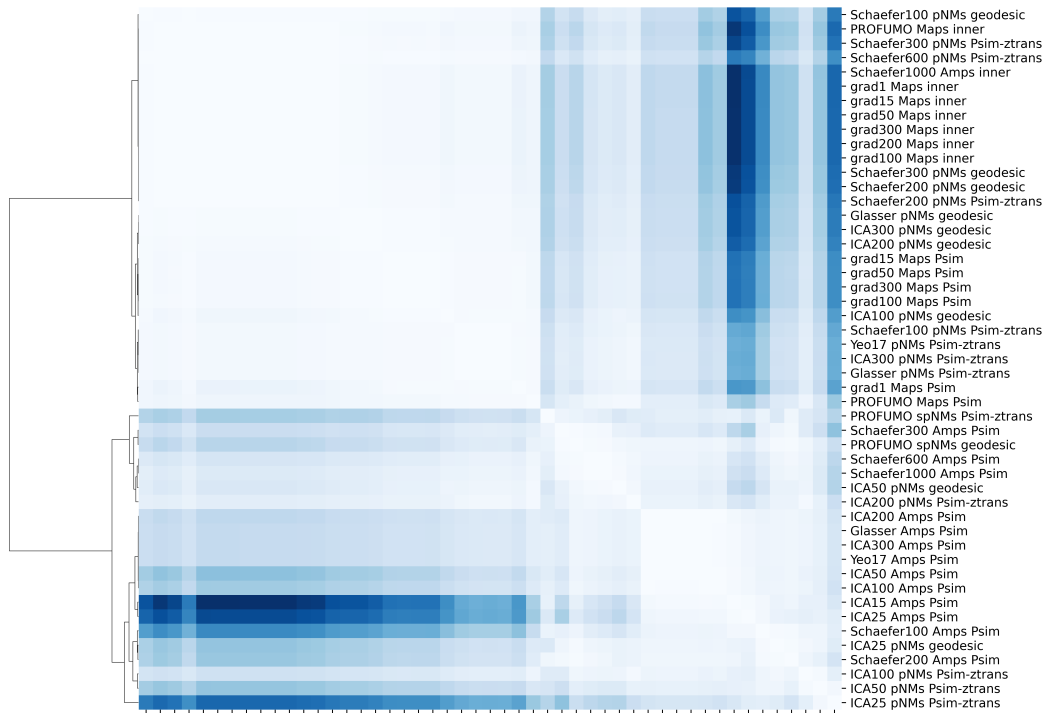
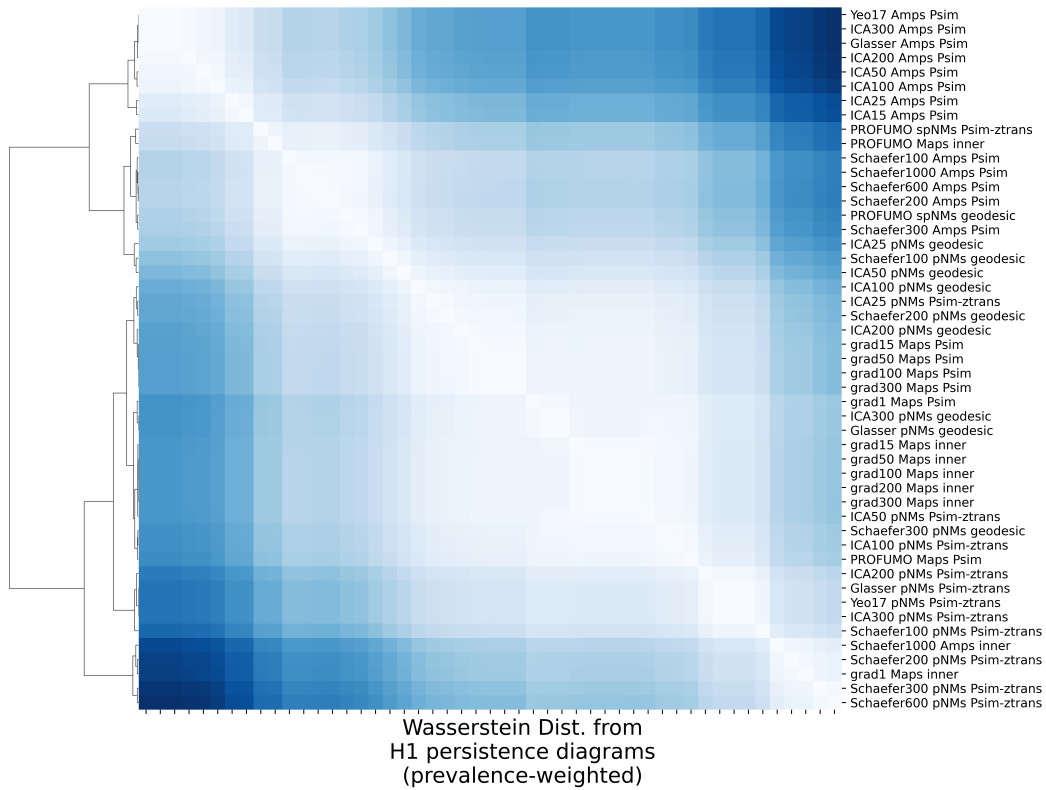


Figure B.4: Clustermaps between all methods from the Wasserstein-2 distance (**Top**) and its prevalence-weighted variant (**Bottom**). The prevalence-weighted distance shows greater differentiation between methods.

Parameter subsets with trivial H_1 structure:

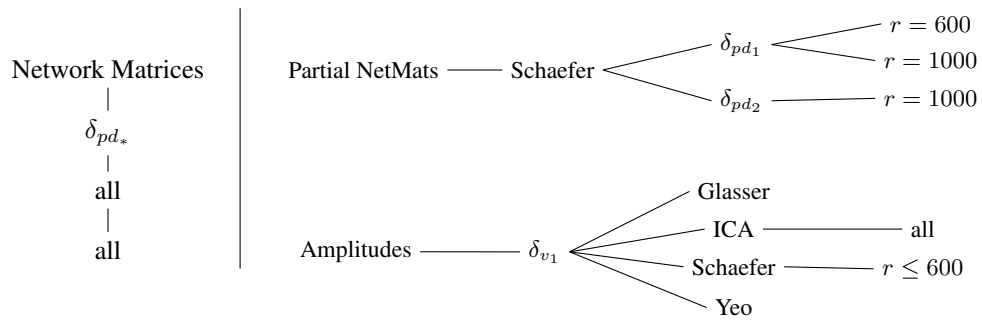


Figure B.5: Tree structure delineating the full set of combinations of brain representation, decomposition rank parameters, feature types, and dissimilarity functions that gave trivial results. – will turn this into a pretty tree later.